COMPUTATIONAL INVESTIGATION OF SHOCK-SHOCK INTERACTIONS AT MACH 6

Michelle L. Jones, Alireza Mazaheri
NASA Langley Research Center, Hampton, VA, 23681

The effects of fin sweep angle on peak heating rates due to shock-shock interactions were simulated at conditions corresponding to the NASA Langley Research Center 20-inch Mach 6 Air Tunnel. The fin angle of attack was varied from 0° (normal to the free-stream) to 15° and 25° swept forward. Global heat transfer data was available for comparison, obtained using a phosphor thermography measurement technique.

The results were obtained using the Langley Aerothermodynamic Upwind Relaxation Algorithm. A structured grid was used to model the flow in front of a semi-cylindrical geometry with a leading edge radius of 0.25 inches. A planar incident shock was assumed at 16.7° in the simulated boundary conditions of the flow to induce a shock-shock interaction on the swept fin. Computed numerical schlieren data from a time-accurate simulation was compared to high-speed experimental zoom schlieren data to assess the features and the temporal unsteadiness of the shock-shock interactions. Computed streamlines from the numerical simulations were compared to the surface patterns from experimental oil flow models. The heat transfer due to the shock-shock interactions from the numerical simulations was compared qualitatively to contour maps of the one-dimensional semi-infinite heat transfer coefficients derived from the experimental data. The results appear to be in good agreement between the computational and experimental data for the investigated shock-shock interactions.

Variables
c_h = convective heat transfer coefficient (kg/m^{2}s)
h = enthalpy (kJ/kg)
M = Mach number
P = pressure (psi or psia)
$\dot{q}$ = rate of heat transfer (W)
q_{conv} = convective heat flux (W/cm^2)
Re = Reynolds number
U = velocity (m/s)
t = time (s)
T = temperature (°F or K)
z = lateral direction in cylindrical coordinates
ρ = density (slug/ft^3)

Subscripts:
aw = adiabatic wall
w = wall (surface of test article)
FR = Fay-Riddell
t,1 = reservoir stagnation
tw = tunnel wall
∞ = free-stream conditions

Acronyms
AoA = angle of attack
BL = boundary layer
BS = bow shock
CAD = Computer-Aided Design
CFD = Computational Fluid Dynamics
DPLR = Data Parallel Line Relaxation
EF = expansion fan
EDM = Wire Electrical Discharge Machine
GASP = General Aerodynamic Simulation Program
IHEAT = Imaging for Hypersonic Experimental Aeroheating Testing
IS = incident shock
LAL = Langley Aerothermodynamics Laboratory
LaRC = Langley Research Center
LAURA = Langley Aerothermodynamic Upwind Relaxation Algorithm
NASA = National Aeronautics and Space Administration
NASP = National Aero-Space Plane
RCC = Reinforced Carbon/Carbon
RS = reflected shock
Scramjet = Supersonic combustion ramjet
SG = shock generator
SL = shear layer
TP = triple point
TPS = Thermal Protection System
UV = ultra-violet (radiation)
1D = one-dimensional
2D = two-dimensional
3D = three-dimensional

1. Introduction

Commercial, government and military applications rely on research into safe, reliable hypersonic technology. Access to space, planetary entry vehicles, and advanced long-range weapons are just a few of the areas in which hypersonic flight is a key topic of research [1]. Vehicles designed to fly at hypersonic speeds, such as the Space Shuttle Orbiter and planes with integrated ramjet or supersonic combustion ramjet (scramjet) engines, can be subjected to a phenomenon called shock-shock interactions that cause significant, localized surface temperature and

pressure augmentations [2]. Interactions between the vehicle bow shock and the shock around a strut or a wing leading edge can compromise the vehicle's structural components in the absence of protective measures. Numerous computational simulations have investigated shock interaction behavior and heating effects that occur in the hypersonic flight regime to aid in the development of sufficient Thermal Protection Systems (TPS).

Shock-shock interactions in hypersonic flow, as described in this study, involve an oblique incident shock that intersects a bow shock around a blunt body. Edney [2] identified six types of interactions between bow shocks around blunt bodies and incident shocks as shown in Figure 1. The relative angle between the incident shock and the bow shock, as well as the strengths of these two shocks, dictate the features of the resulting shock impingement, such as the angle of the reflected shock, the number of shear layers that form, or the presence of a supersonic jet.

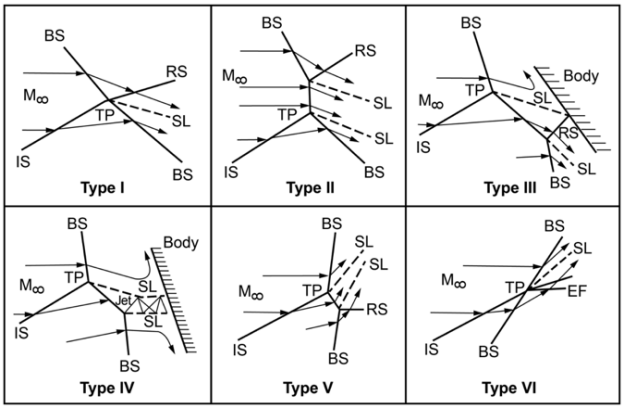

Figure 1. Edney catalogued six shock interaction types, IS = incident shock, BS = bow shock, RS = reflected shock, EF = expansion fan, TP = triple point, SL = shear layer.

In the current study, Type III and Type IV (both direct and glancing, or Type IVa) shock-shock interactions were investigated. Edney [2] states that the peak heating associated with a Type III interference is attributed to a free shear layer attaching to the body, much like in separated flows. The flow between the bow shock and the shear layer is supersonic in this type of an interaction for a blunt body. The Type IV interaction yielded the highest peak heating augmentation in Edney's study. In this interaction, a supersonic jet either curls upward (as in a Type IVa interaction) or impinges directly on the blunt body as in Figure 1. Reflected shocks between two shear layers in this supersonic jet produce shock triangles that are also referred to as a "shock train."

The necessity of considering heating augmentation due to shock-shock interactions is evident in real flight scenarios, as reference [3] describes. Several shock-shock interaction studies focused on the two-dimensional (2D) shock-on-cowl interaction in which a planar incident shock intersects the bow shock around a cowl leading edge that is parallel to the plane of the incident shock (as in [4], [5], [6], [7]). The current test set-up simulates a three-dimensional (3D) "shock-on-fin" interaction due to an intersection between a bow shock around an aircraft fuselage and the shock around a strut (fin) leading edge. These interactions on a hypersonic vehicle are shown in Figure 2.

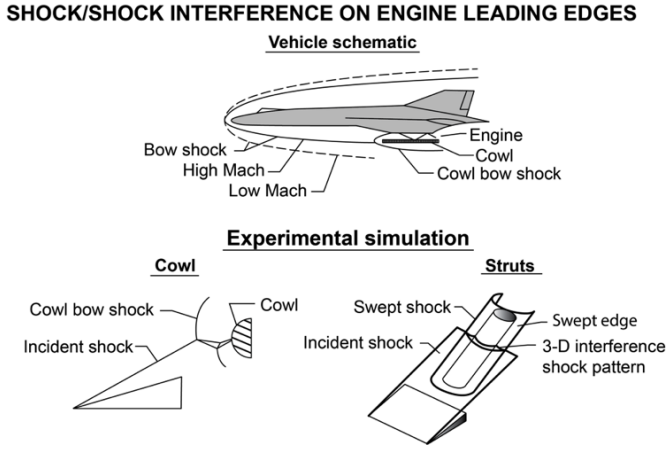

Figure 2. Shock-on-cowl and shock-on-fin types of shock-shock interactions.

Wright et al. [8] conducted numerical simulations using the General Aerodynamic Simulation Program (GASP) and the Data Parallel Line Relaxation (DPLR) CFD codes for flow conditions and test article geometries similar to the Berry and Nowak experimental study [9]. In particular, Wright et al. used structured cylindrical meshes with spherical caps at either end to approximate the geometry of a 0.25 in-radius test article leading edge. Although the actual model has sharp corners at the extreme locations on the leading edge, this grid shape is acceptable because the edge effects do not impact the heat flux in the shock-shock interaction region. Wright et al. ran the CFD code with the grid inclined at 0°, -15° and -25° to the Mach 6 flow, as in the current study, assuming an ideal planar shock angle of 16.75° for the incident oblique shock. The simulations in the Wright et al. study were not time-accurate, but instead yielded averaged solutions over several iterations.

These CFD simulations predicted a peak augmentation of 8 for the -15° angle of attack (AoA) or "15° forward swept" Type IV interaction, 6.5 for the -25° AoA Type III interaction, and only 1.6 times the baseline value for the 0° AoA Type IVa interaction. Wright et al. calculated the density gradients in the flow around the cylindrical fin based on the computed flow field and compared these results to the experimental zoom schlieren data from [9]. Computed schlieren images for the Type III and Type IV shock-shock interactions are shown in Figure 3. The middle image in this figure is clearer because the Type IV interaction image was scanned from an original image with Wright's permission, rather than from the figure in [8]. Similar numerical schlieren calculations were performed using the Langley Aerothermodynamic Upwind Relaxation Algorithm (LAURA) code [10] in the current study. The computational streamline data in Figure 4 suggest vortices are present in the flow for Type III and IV interactions that correspond to -15° and -25° test article angles of attack.

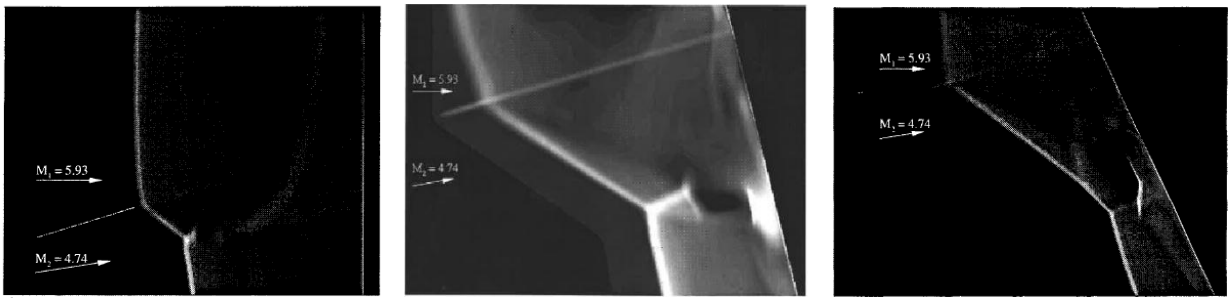

Figure 3. Computed schlieren data for the shock-shock interaction region on a 0.25 in-radius test article at a 1) 0° AoA, 2) -15° AoA, and 3) -25° AoA (from left to right) in approximately Mach 6 flow [8].

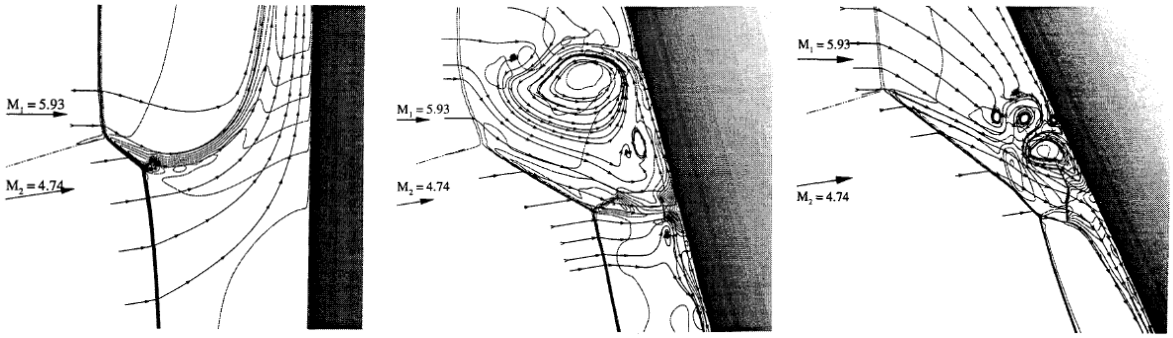

Figure 4. Streamlines and density contours for the shock-shock interaction region on a 0.25 in-radius test article at a 1) 0° AoA, 2) -15° AoA, and 3) -25° AoA (from left to right) in approximately Mach 6 flow [8].

The results of the current study contribute to the knowledge of 3D shock-on-strut interactions in hypersonic flight. The LAURA computational outputs for the three flow configurations were used to obtain numerical schlieren, heat transfer contour maps and streamline patterns for each case. These sets of data are compared qualitatively to experimental global heat transfer data, images from high-speed zoom schlieren videos and oil-flow images.

2. Computational and experimental set-up

The effects of the fin leading-edge radius and sweep angle on peak heating rates due to shock-shock interactions were investigated in the NASA Langley Research Center 20-inch Mach 6 Air Tunnel [11]. This tunnel [12] is a perfect gas facility that has well-characterized flow uniformity and composition [13]. The fin model leading edges, which represent cylindrical leading edges or struts on hypersonic vehicles, were varied from 0.25 inches to 0.75

inches in radius. A 9° wedge generated a planar oblique shock at 16.7° to the flow that intersected the fin bow shock, producing a shock-shock interaction that impinged on the fin leading edge. The fin angle of attack was varied from 0° (with the leading edge normal to the free-stream) to 15° and 25° swept forward. Global temperature data was obtained from the surface of the fused silica fins using phosphor thermography. Metal oil flow models with the same geometries as the fused silica models were used to visualize the streamline patterns for each angle of attack. High-speed zoom-schlieren videos were recorded to show the features and temporal unsteadiness of the shock-shock interactions. The temperature data were analyzed using one-dimensional semi-infinite as well as one- and two-dimensional finite-volume methods to determine the proper heat transfer analysis approach to minimize errors from lateral heat conduction due to the presence of strong surface temperature gradients induced by the shock interactions. The general trends in the leading-edge heat transfer behavior were similar for the three shock-shock interactions, respectively, between the test articles with varying leading-edge radius. Additional information about the test article fabrication, the data acquisition processes and the run matrix for this study is provided in [11].

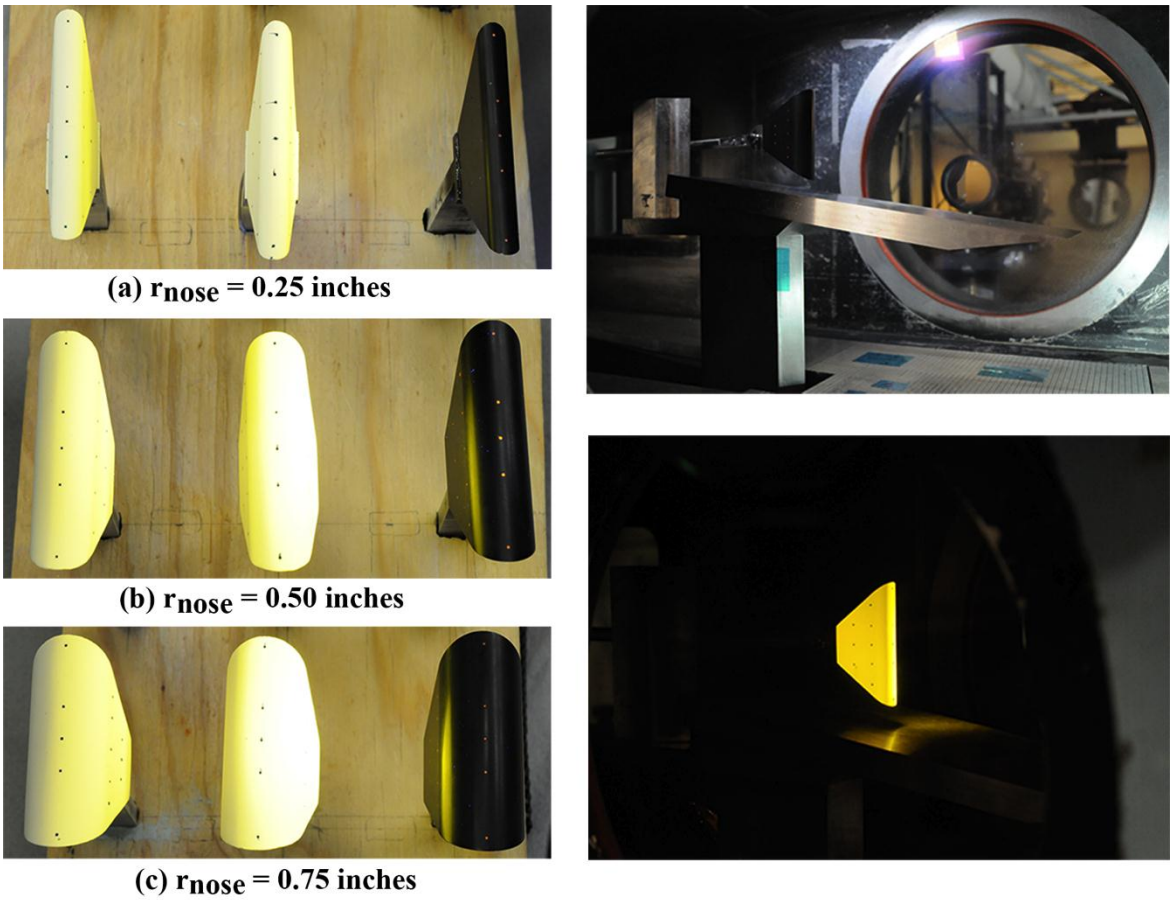

Figure 5. Left image: Primary and back-up fused silica test articles and metal oil flow test articles from experiment in [11]. Right images: Metal test article (0.75 in-radius, top) and fused silica test article (0.50 in-radius, bottom) inserted in the tunnel with 360 nm UV illumination.

A preliminary CFD simulation was conducted in LAURA assuming Mach 5.96, laminar flow to approximate the boundary layer thickness over the flat plate shock generator (SG) [11]. A grid was generated in Pointwise® to represent the 17 in-long flat plate with a sharp leading edge angled at 9° to the flow. The simulation showed the maximum boundary layer thickness at the back of the plate is 2 mm or 7.9×10^{-2} in. Based on this result, a separation of 0.5 in between the lower tip of the test article and the flat plate SG was deemed sufficient to ensure that the flat plate boundary layer does not interact with the flow over the test article for a 0.25 in-radius test article. This approximate separation was maintained in the wind tunnel experiment in [3].

The simulation matrix in Table 1 shows the three shock-shock interactions that were modeled computationally in this study. The size of the grids used in the simulations is listed in terms of the number of cells in the i, j, and k dimensions. In this coordinate system, the "i" component corresponds to the direction around the circumference of

the test article from the stagnation line toward the centerline of the leading edge, the "j" component is the lateral direction down the leading edge, and the "k" component points out from the surface of the test article. "Coarse" grids were used in the initial simulations in each case to obtain a solution with a converged bow shock, and the "fine" grids were used after the incident shock was added to model the flow for the Type III, IV, and IVa shock-shock interactions.

The grid used for the 0° AoA case only contains 48 blocks, compared to 69 blocks for the other two cases. An image of this grid is included in Figure 6 for reference. The increased resolution near the shock-shock interaction region in the 69-block grid slowed the propagation of the free-stream flow for this case while the bow shock was set up in the coarse grid, which prevented the bow shock from converging to the correct shape. The other difference between the grid dimensions stems from a change to include a small radius (0.1 in) at the top of the leading edge for the 0° AoA simulation (which was conducted after the other two simulations) that ensured the bow shock was detached from the leading edge. This additional radius extended the length of the leading edge beyond the 4 in of the actual test article, which likely did not greatly affect the simulation since edge effects are sufficiently far away from the shock-shock interactions for the 0.25 in-radius test article.

Table 1. Simulation matrix.

Type of Interaction	Leading Edge AoA	Coarse Grid Size (i x j x k)	Fine Grid Size (i x j x k)	Number of blocks in the grid
IVa	0°	37 x 251 x 251	73 x 501 x 501	48
IV	-15°	37 x 369 x 255	73 x 737 x 511	69
III	-25°	37 x 369 x 255	73 x 737 x 511	69

IHEAT [14] was used to convert the phosphor intensity images of the test articles in [3] to surface temperatures as well as to obtain surface heat transfer coefficients. IHEAT is a one-dimensional (1D) code that assumes the test article is semi-infinite in the through-thickness dimension, so heat applied at the surface does not reach the back of the test article during a short wind tunnel run. Heat transfer coefficients, c_h, are calculated from a convective heat transfer, $\dot{q}_{conv}$, equation based on an enthalpy difference between the adiabatic wall enthalpy (h_{aw}) and the wall enthalpy (h_w), ie.,

$$\dot{q}_{conv} = c_h(h_{aw} - h_w) \tag{1}$$

Additional assumptions and equations incorporated in the IHEAT code are described in [14] and [15]. Uncertainties in the phosphor thermography data depend on the rise in the test article surface temperatures. On surfaces with a significant temperature rise (>70ºF), uncertainties are in the range of ±10%. For moderate temperature increases (20-30ºF), the uncertainties are roughly ±25%. More information on phosphor thermography uncertainties is found in [14] and [15].

The LAURA code was modified to simulate the flow behavior necessary for shock-shock interactions similar to the experimental configurations. An additional boundary condition permits a second set of flow conditions to be specified for flow that would pass through the incident shock. Using the Pointwise® grid generation program and a CAD model of the 0.25 in-radius test article, meshes were created with higher grid resolution in the expected shock-shock interaction region. The grids extend from the stagnation line on the leading edge around the circumference to the centerline of the nose of the test article, and extrude about 0.5 in into the free-stream flow as shown in Figure 6, with a slice at the stagnation line and a zoomed-in view (in the red box) of the boundary layer near the rounded tip.

Initial simulations were run with Mach 5.96, perfect gas flow parameters set in LAURA to obtain a converged solution of the test article bow shock for each case. Then, additional parameters were set to simulate the conditions in the free-stream flow behind a 16.7° incident shock produced by the flat plate SG [16]. These conditions are listed in Table 2. The pitch angle of the flow in the table is specified relative to the x-axis in Figure 6. Simulations were completed using the smallest test article geometry (a 0.25 in leading-edge radius) from the experiment in [3].

Table 2. Flow properties above and below the incident shock (IS) due to the SG angle [16].

Flow passes through IS	U (m/s)	Flow angle (degrees)	T (K)	ρ (kg/m^3)
No	944.9	-180.0	62.5	0.03195
Yes	913.9	-196.7	91.8	0.07090

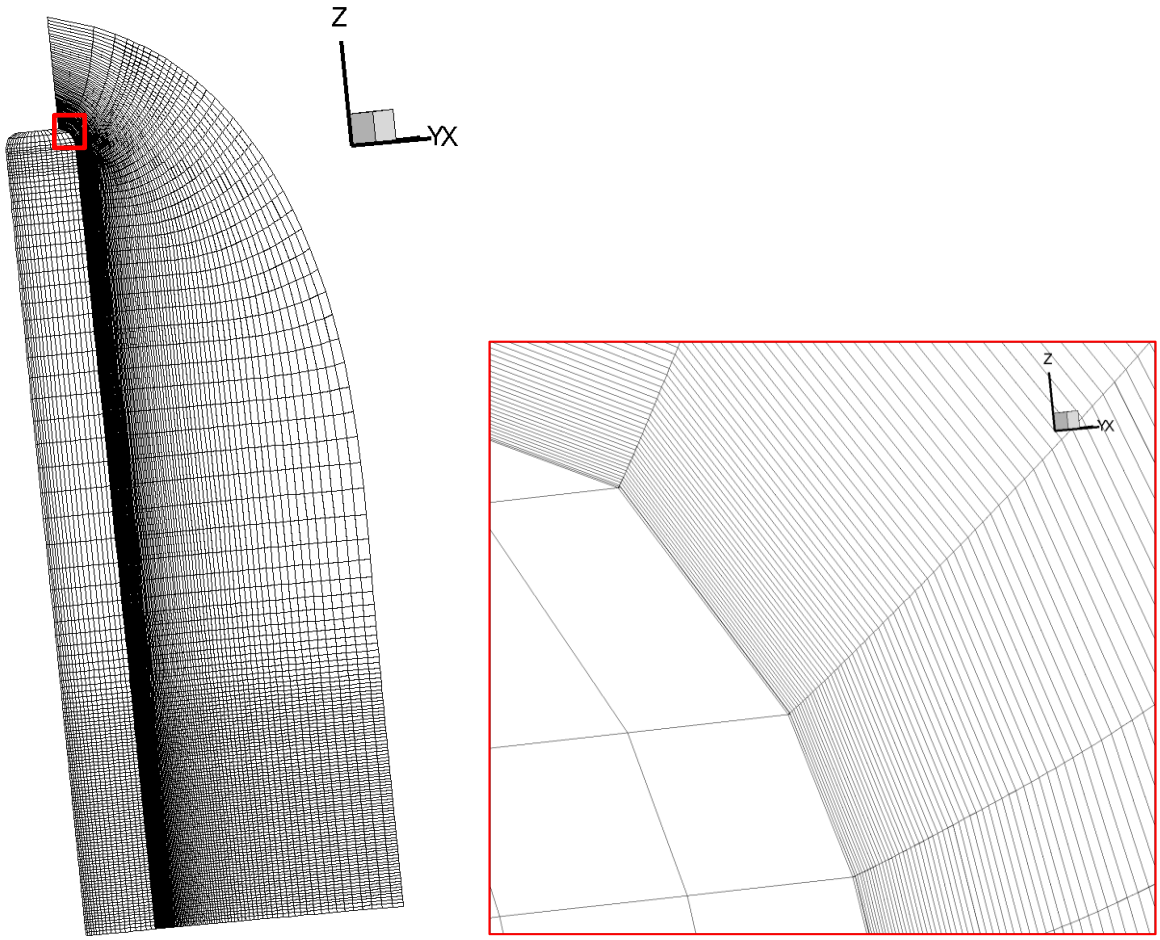

Figure 6. Grid for the 0° AoA case with a radius of 0.1 in added to the top tip of the leading edge to ensure a detached bow shock. Grid is coarsened by a factor of 4 in i, j, and k directions, with a zoomed-in view of the boundary layer in the red box (right image).

3. Results

Heat transfer, schlieren, and streamline data based on the CFD outputs are presented to assess the effects of the shock-shock interactions and to visualize these flow phenomena for a 0.25 in-radius fin swept 0°, -15°, and -25°. These sweep angles provide two cases with strong lateral temperature gradients due to the Type IV (at a -15° AoA) and the Type III (at a -25° AoA) shock-shock interaction regions, and one lower heating case for a Type IVa interaction (at a 0° AoA). These results are qualitatively compared to experimental results from similar test configurations in [3]. The shock-shock pattern is more clearly distinguishable in the zoom schlieren images for the 0.75 in-radius test articles in [3] since the bow shock standoff distance is greater. Since the same features of the shock-shock interactions appear in the zoom schlieren and oil flow images for the three test article radii in [3], the images for the 0.75 in-radius test article are used in those comparisons in later sections.

3a. Computational versus experimental heat transfer

The images in Figures 7 through 10 compare representative snapshots of the computed surface heat transfer patterns on a cylinder from LAURA to IHEAT contour maps of the 1D Fay-Riddell [17] non-dimensionalized heat transfer coefficients. The IHEAT contour maps are shown for zoomed-out and zoomed-in views at a time t = 1.8 s into the run. The limits on the color bar scales for the images based on the CFD and experimental data are kept constant to ensure the main features of the heat transfer pattern are visible for every test configuration. Since the plotted parameters differ, only the overall heating patterns are compared in these images.

Heat transfer images from the time-accurate LAURA simulations were compiled into videos. Only half of the cylindrical leading edge is included in these simulations, since the heat transfer is symmetric on the other side of the stagnation line (located on the right edge of the displayed geometry). The mesh is not shown in these images to

avoid obscuring the features of the heat transfer. The leading edges for the LAURA cases have been rotated to a vertical orientation in the last two cases to view the contour maps more clearly. Since the shock-shock interaction typically affects a localized region on the lower half of the test article geometry, the image of the leading edge heat transfer contours from LAURA shows a zoomed-in view rather than the full leading edge.

Figure 7 shows the LAURA and IHEAT contour maps based on the heat transferred to the 0.25 in-radius test article at a 0° AoA. The LAURA images show a straight-on view of the half leading edge, while the IHEAT images are captured at an angle through the wind tunnel window. In these images, an elevated heating region exists above the shear layer attachment point on the leading edge. This region spreads farther around the circumference of the test article near the interaction region and is narrower farther up the leading edge. Also, both sets of images reveal higher amounts of heat are transferred to the lower segment of the leading edge (below the shear layer attachment), likely due to lateral conduction along the leading edge as well as the higher temperature of the flow that passes through the incident shock before contacting the surface of the test article.

The half ellipses that end at the stagnation line in the LAURA image in Figure 7 correspond to peaks in the heat transfer coefficients on the leading edge. The light blue peaks below the yellow peak are likely due to the non-physical phenomena associated with a region of unusual flow parameters in the simulation. These unexpected flow properties appear in a triangular region in the stagnation plane between the incident shock and a horizontal line. This wedge of unusual free-stream flow is discussed in more detail in the description of the numerical schlieren images.

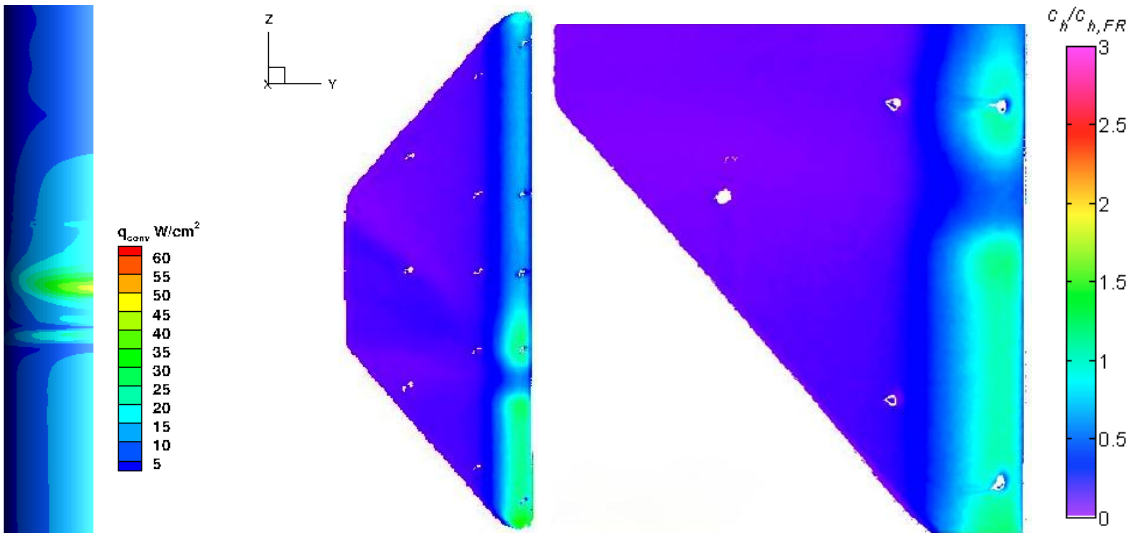

Figure 7. Heating pattern on the leading edge of the 0.25 in-radius test article at a 0° AoA (left), compared to two IHEAT $c_h/c_{h,FR}$ heat transfer coefficient contour maps (middle and right).

The contour maps in Figure 8 correspond to a Type IV interaction on the 0.25 in-radius test article at a -15° AoA, both from LAURA (left image) and IHEAT (right two images). The shock interaction wraps around the test article, creating streaks of higher heating coefficients on the side, as shown in the IHEAT contour maps. A narrow peak on the leading edge in all three images corresponds to the point where the supersonic jet impinges on the test article. Again, in both sets of data the heat transfer to the lower part of the test article is higher than that above the shock-shock interaction region, as is most evident in the zoomed-out heat transfer mapping from IHEAT.

The unsteadiness above the narrower peak heat transfer is evident in the video compiled from LAURA heat transfer images, although this phenomenon is not shown in the figure. The pale blue regions above the peak in the LAURA image change shape over time, possibly due to a region of fluctuating density in the flow above the incident shock [3]. A nearly circular region of elevated heating wraps around the leading edge in the same location above the supersonic jet in the IHEAT contour maps. In the IHEAT images, the heat transferred to this region is relatively uniform over time, which suggests phosphor thermography provides mean heat transfer coefficients that do not capture the effect of the unsteadiness in the flow, possibly due to the response time of the phosphor coating.

Both CFD and phosphor thermography reveal the Type IV peak heating region is relatively stable, i.e. the peak does not disappear or move around much in the sequential images. This result is expected from the behavior of the supersonic jet in the numerical and experimental schlieren, which is discussed in the next section. The blue striations below the peak on the leading edge in the left image correspond to small vortices in the LAURA simulation that move down the leading edge as the simulation progresses.

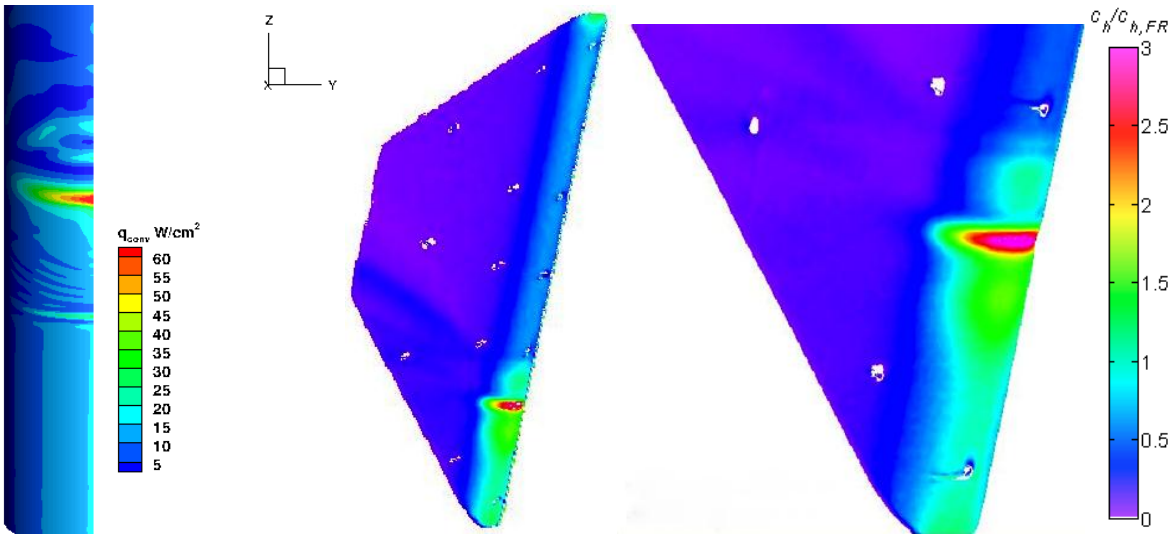

Figure 8. Heating pattern on the leading edge of the 0.25 in-radius test article at a -15° AoA (left), compared to two IHEAT $c_h/c_{h,FR}$ heat transfer coefficient contour maps (middle and right).

A Type III shock-shock interaction produces a broader peak heat transfer region than the peak for the Type IV interaction, as the images in Figures 9 and 10 show. The heat transfer images for the -25° AoA case in Figure 9 show unsteadiness along the leading edge in the interaction region, from just above the broad peak due to the shear layer attachment down to the lower tip of the test article. These four representative images correspond to every third image from data recorded at 40 Hz (although the time step in the simulation is Δt = 1e-4s). The peak at times disappears and bounces around in the video compiled from several consecutive images, which agrees with the numerical and experimental schlieren evidence of the shear layer attaching and detaching from the surface of the test article (as shown in the following section). Features below the broad peak in the images travel down the leading edge during the video, possibly due to the vortices in the numerical schlieren images.

IHEAT contour maps for the 0.25 in-radius test article at a -25° AoA are included in Figure 10. The effects of the shock interaction again wrap around the test article, creating streaks of higher heating on the side of the test article. Heat transfer coefficients derived from phosphor thermography images appear to represent an averaged value in this case as well, since the effect of vortices is not evident in the apparently uniform region of higher heat transfer coefficients below the peak.

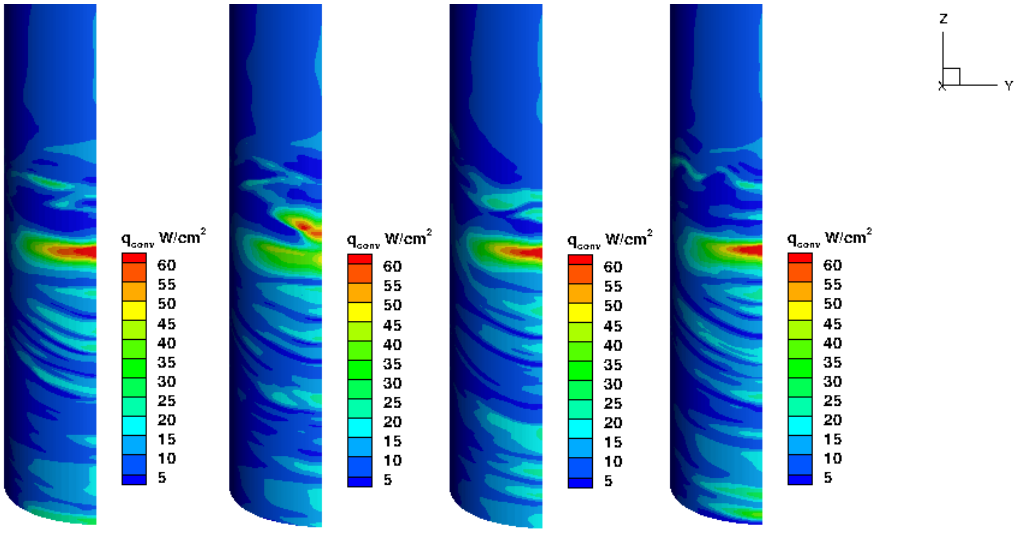

Figure 9. Heating patterns on the leading edge of the 0.25 in-radius test article at a -25° AoA in every third image generated from the output at 250 Hz early in the LAURA simulations.

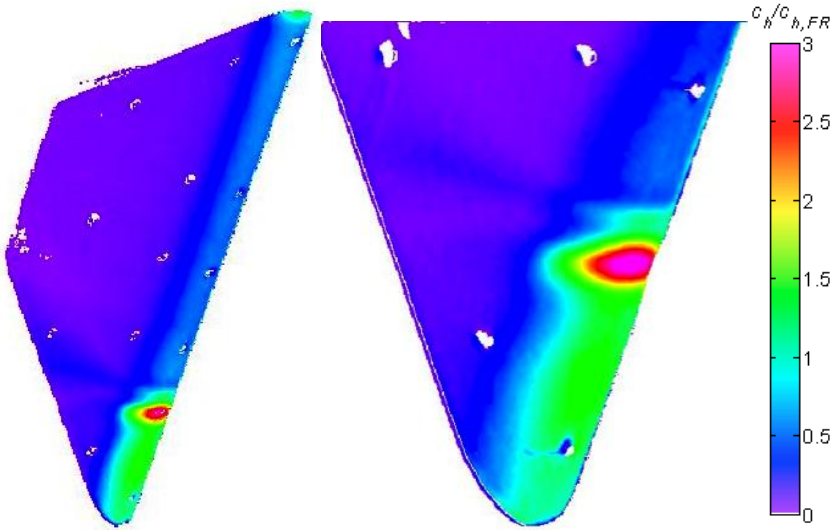

Figure 10. IHEAT $c_h/c_{h,FR}$ contour maps for the 0.25 in-radius test article that are 1) zoomed out (left) and 2) zoomed in (right) at a -25° AoA.

3b. Numerical schlieren versus experimental schlieren

Figure 11 displays images from [3] of the 0.75 in-radius test article at a 0°, -15° and -25° AoA (from left to right). In the Type IVa interaction in the left image, a narrow supersonic jet extends at an angle from the triple point to the location where the bow shock is again nearly vertical, before turning to travel almost horizontally to an impingement point on the surface of the test article. A pattern of triangles that comprise the shock train formed by reflected shocks is visible near the beginning of the supersonic jet. The shear layer above the shock train curves up toward the incident shock, as evidenced by a darker region in the density gradients, which is clearer in the videos.

A supersonic jet emanates from the triple point and impinges nearly perpendicularly on the surface of the test article for the Type IV interaction as the middle image in Figure 11 shows. The schlieren videos of this interaction reveal changes in the density of the air between the bow shock and the test article surface above the extrapolated incident shock location over time. However, the density gradient in that region is not as clear in the still image.

In the Type III interaction, the supersonic jet of the previous two interaction types is replaced with a shear layer that attaches to the surface of the test article. Supersonic flow exists in the triangular region between the turned bow shock and the shear layer in the image [2]. Although the shear layer attachment point is not clearly evident in the zoom schlieren images, the shear layer leaves the triple point with the incident and bow shocks at the appropriate angle to connect to the test article surface at the same location as the reflected shock. An unsteady region between the test article surface and the shear layer near the attachment point (labeled as a density gradient in the right image, although this phenomenon is clearer in the schlieren video) contributes to the difficulty in capturing the shear layer attachment in a still image.

Equation (2) is used to calculate the flow density gradients in Tecplot with output data from the LAURA simulations for time-accurate simulations of the two shock-shock interactions. This calculation is called "numerical schlieren" because the changes in the free-stream flow density from a numerical simulation of a given shock-shock interaction are shown as visual density gradients similar to the output for the experimental schlieren technique. This numerical schlieren expression is derived for the case with the test article at a -25° AoA, and is applied to the -15° AoA case to obtain reasonably clear density gradients, as given by

$$\text{Numerical schlieren} = exp\left(\frac{-200 Density\ Gradient\ Magnitude}{189808}\right) \tag{2}$$

A similar equation is applied for the 0° AoA case with the denominator set equal to 26509 to provide better contrast in the flow density features. The modified equation also yields much darker density gradient contours on the surface of the vertical leading edge for the 0° AoA case. The zoomed-in numerical schlieren images in Figures 12 through 14 are derived from LAURA output data for a cylindrical model of the leading edge of the 0.25 in-radius test article at the appropriate angle of attack. The density gradients both on the surface of the test articles and in a slice perpendicular to the leading edge (along the stagnation line) are shown in these images.

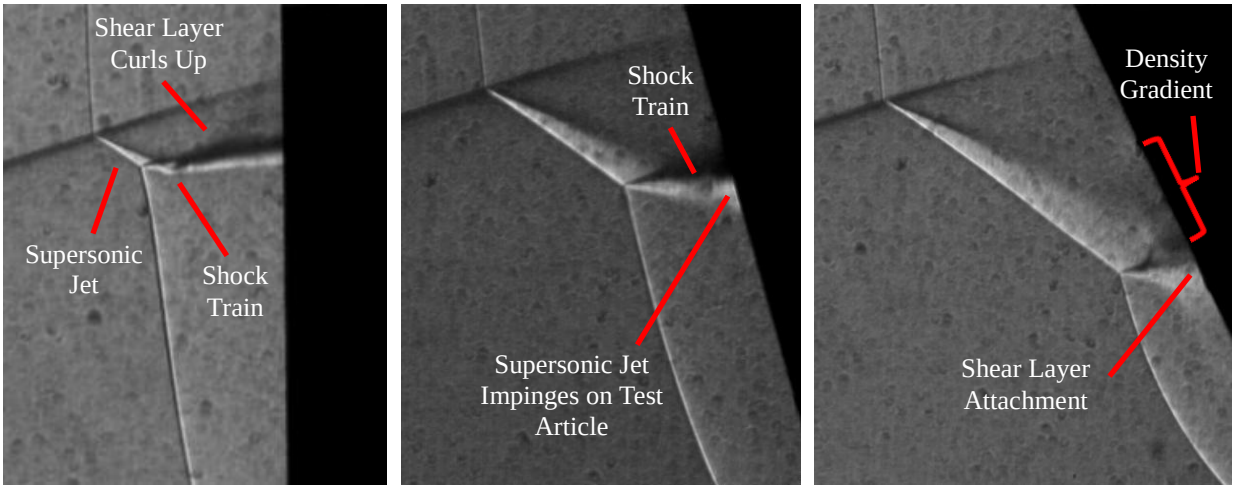

Figure 11. Zoom schlieren images of the 0.75 in-radius test article at a 0°, -15° and -25° AoA (from left to right) from reference [3].

The images in Figure 12 for the Type IVa interaction are shown in consecutive order from times near the beginning of the time-accurate simulation. This simulation was conducted with the incident shock originating from a lower point relative to the leading edge compared to the heat transfer and streamline images to utilize the increased spatial grid resolution for the interaction region. The bow shock and the incident shock are labeled in images a and b as the shock-shock interaction flow is set up. A horizontal line in these images also exists in the other simulations, though the line is not evident in those images, possibly due to the contrast levels inherent in the numerical schlieren equation. This line only has a noticeable effect on the flow within the bow shock for the Type IVa interaction, producing non-physical density gradients. The shear layer labeled in image f curls up before attaching to the leading edge, and a small supersonic jet is visible in later images (such as image i), as expected for a Type IVa interaction.

Although the images are obtained in consecutive order during a time-accurate solution, frames at arbitrary times are included in Figure 13 to show the progression of the Type IV simulation over time. The images labeled a through d show an unsteady density gradient circling above the incident shock that resembles the circular density gradient in the experimental zoom schlieren for this type of interaction. Unlike in the experimental schlieren, the later images in this figure show this density gradient eventually diminishes, which suggests the grid resolution in that region may not be sufficiently fine for the CFD simulation to capture the persistence of that flow phenomenon as time progresses. These images also show small vortices traveling down near the leading edge of the test article, which are not visible in the experimental zoom schlieren, but these flow features also disappear later in the time-accurate simulation. In images g through i, the shock triangles of the supersonic jet are clearly distinguishable.

The images in Figure 14 for the Type III interaction are shown in consecutive order from the time-accurate simulation. From this small segment of time, the reflected shock that impinges on the test article surface bounces around as an unsteady rotating density gradient (shown in all the images) interferes with the shear layer from the triple point, causing the shear layer to attach and detach from the surface. Based on a video compiled from these images, the simulated flow in this rotating region moves up the leading edge near the surface, out from the leading edge toward the shear layer, down through the shear layer, and then back toward the test article surface. This motion agrees with the upward direction of the streamlines on the oil flow images above the attachment of the shear layer in the shock interaction region. The flow below the reflected shock moves in vortices down the leading edge. Only in image g does the shear layer attach to the surface of the test article in these frames for the Type III interaction.

Density gradients in the figures (especially for the two last types of interactions) also wrap around the surface of the test article, as indicated by the heat transfer contour maps and oil-flow images from [3]. Gradients in the flow density behind the test articles in the experimental zoom schlieren suggest these numerical features exist, although changes in flow density on the test article surface cannot be detected by the experimental zoom schlieren method.

In the 2D schlieren images, the planar incident shock is a line that appears to travel inside the bow shock to impinge on the test article leading edge due to the integrating optics of the zoom schlieren system, which project the density gradients in the line of sight onto a 2D image. However, the incident shock shown in the stagnation plane does not continue through the bow shock to impinge on the leading edge in any of the numerical schlieren images. This flow behavior suggests the incident shock intersects the bow shock at the triple point but then wraps around the bow shock with the same slope as the incident shock.

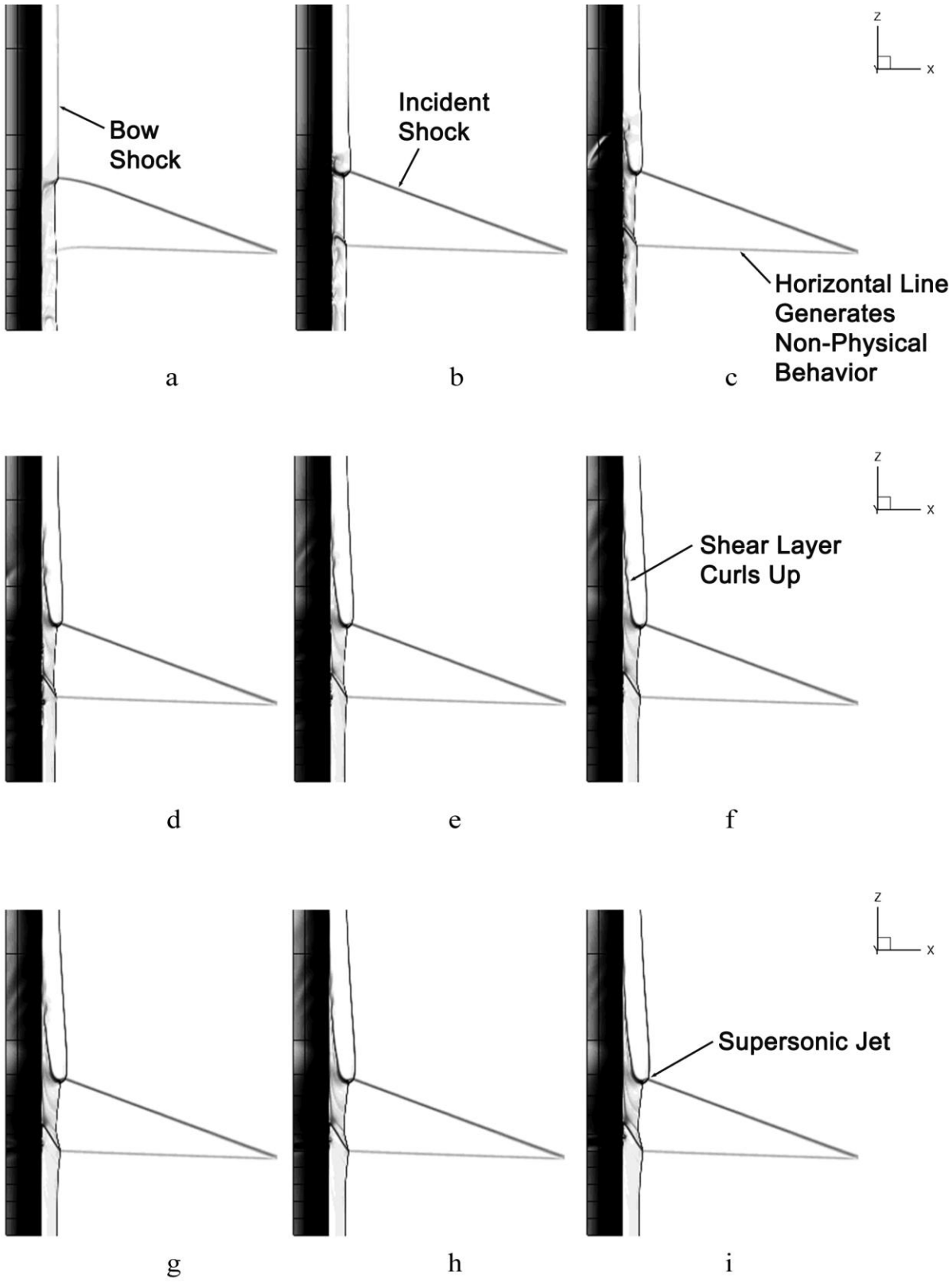

Figure 12. Numerical schlieren images for the 0.25 in-radius test article at a 0° AoA with a 9° SG (samples of consecutive frames early in the time-accurate LAURA simulation).

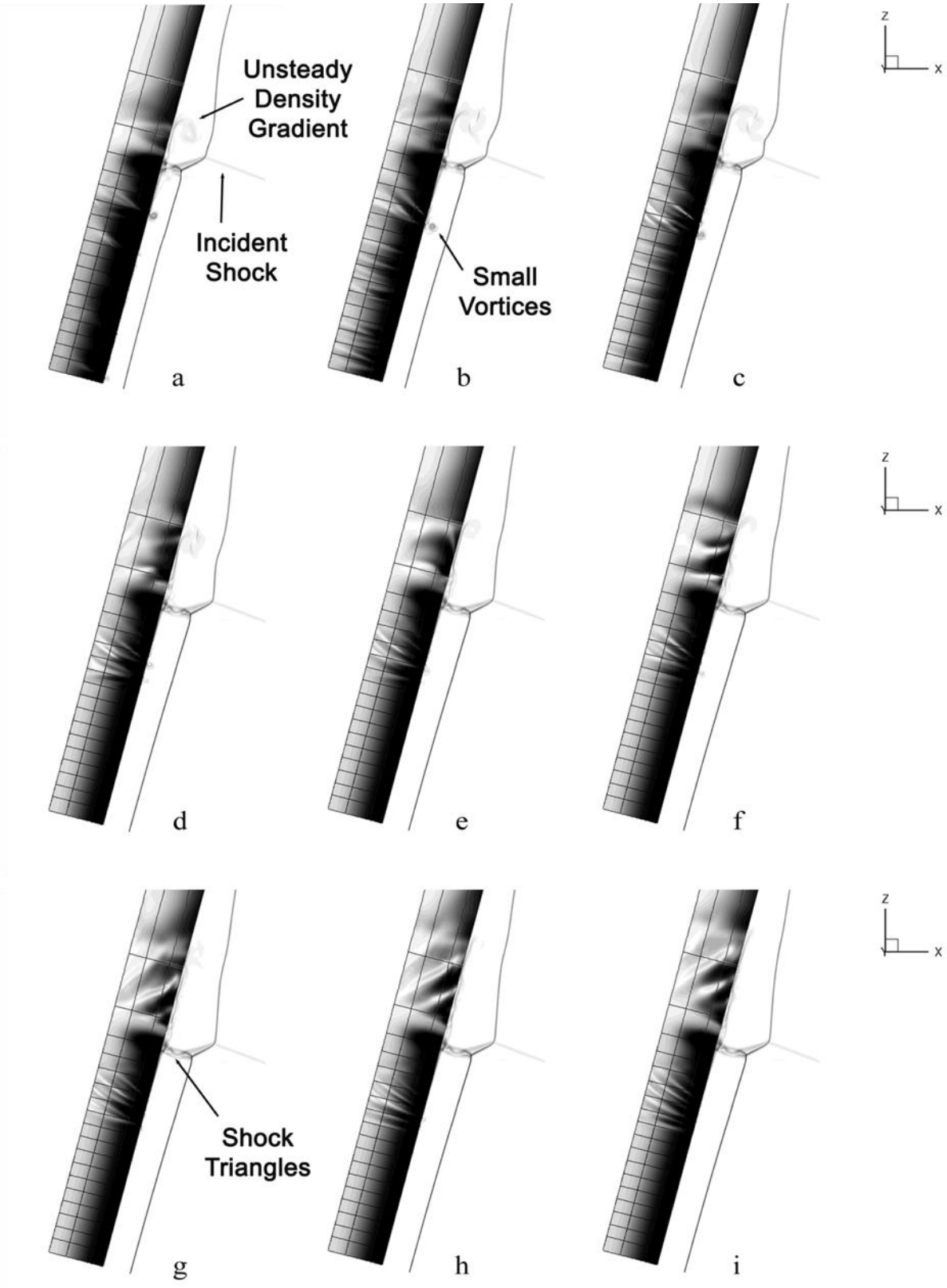

Figure 13. Numerical schlieren images for the 0.25 in-radius test article at a -15° AoA with a 9° SG (samples of non-consecutive frames in the time-accurate LAURA simulation).

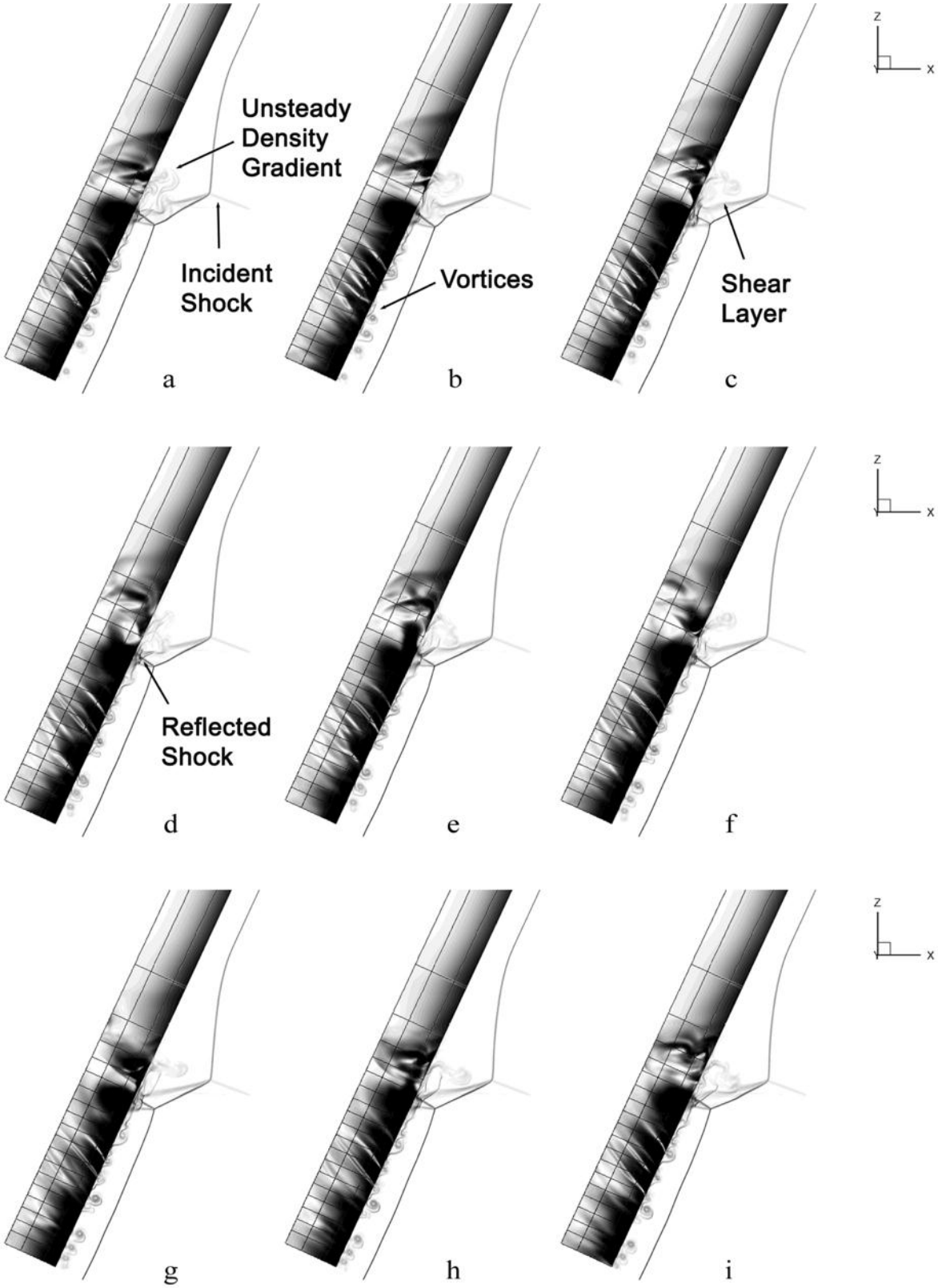

Figure 14. Numerical schlieren images for the 0.25 in-radius test article at a -25° AoA with a 9° SG (samples of consecutive frames in the time-accurate LAURA simulation).

3c. CFD streamlines versus experimental oil flow images

Oil flow images in Figure 15 show characteristic streamlines and shear patterns for this Type IVa interaction with the 0.75 in-radius test article. The features in these oil-flow images are similar to the streamline patterns observed in the 0.25 and 0.50 in-radius test articles. The second image from the left indicates the oil movement for a test article that was initially fully coated with oil, while the other images show streamlines on a test article that was covered with dots of pigmented oil prior to the run. Edney [2] states that a region of dead air exists along the leading edge just below the upper shear layer attachment point in an oil-flow image of a 0.59 in-radius cylinder exposed to a Type IVa interaction. The oil-flow streamlines on the leading edge in Figure 15 exhibit this same behavior. These streamlines also resemble the oil-flow streamlines for a 0.5 in-radius cylinder in [18], with different behavior near the bottom of the leading edge since the test article was separated from the flat plate SG in the current study.

A horizontal line around the circumference of the leading edge in the full-coating image indicates the attachment point of the curved shear layer above the supersonic jet. This line is near the location where the planar incident shock wraps around the test article, as seen in the schlieren images. Streamlines travel upward from the attachment point and then turn away from the leading edge. In the region near the top of the test article, the oil along the stagnation line did not move. The side oil flow patterns are similar as nearly horizontal streamlines flow away from the leading edge and then turn toward the slanted edges of the test article. The bow shock around a test article at a 0° AoA is a nearly normal shock and, thus, the flow above the incident shock does not change direction but instead continues horizontally until the air reaches the surface of the test article.

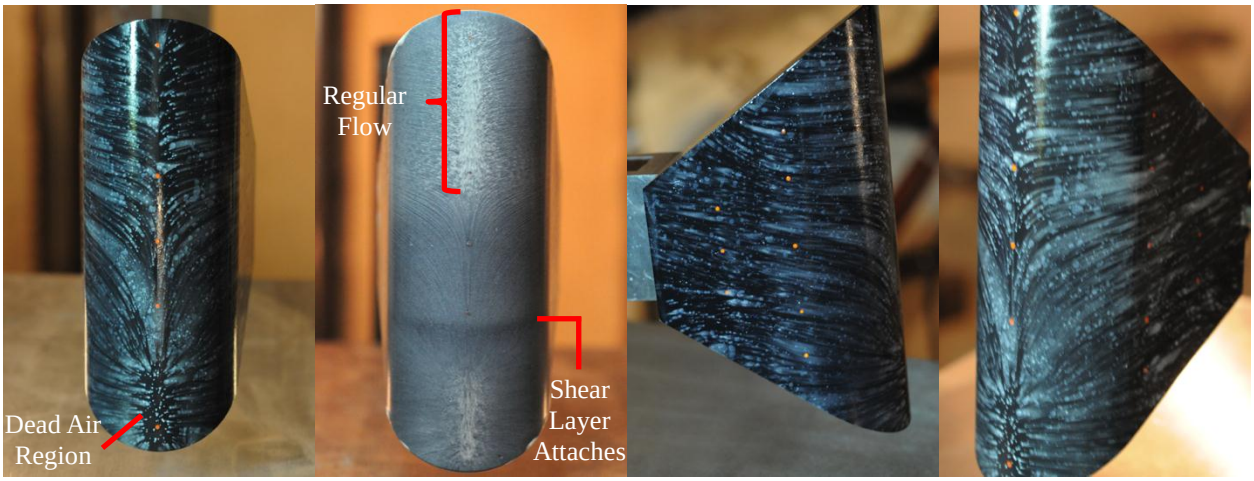

Figure 15. Oil-flow images for the 0.75 in-radius metal test article at a 0° AoA. Numbered from left to right, 1) leading-edge view, dots, 2) leading-edge view, full coating, 3) right side view, dots, 4) left side view, dots.

Blocks of cells in the grid show up as a nearly rectangular grid that wraps around the leading edge on the left side of the two density images in Figure 16, as in the heat transfer plots and numerical schlieren images. A zoomed-in view of the surface of the test article geometry is included in both images. The stagnation plane also is included in the density contour maps, but other planes in the free-stream flow above the surface are hidden. These images show streamlines derived from the CFD simulation in the free-stream flow and on the surface of the test article.

The streamlines near the top of the left image in Figure 16 pass through the bow shock and then travel nearly horizontally around the cylindrical surface away from the stagnation line. Additional streamlines not shown in the zoomed-in images indicate the streamlines farther up in the flow also travel horizontally back from the leading edge. These streamlines match the “regular flow” pattern observed near the top of the leading edge on this test article, shown in Figure 15 for the largest test article geometry in [3]. The upper streamlines on the leading edge are also similar between the CFD and the oil flow images for the -15° and -25° angles of attack (not shown in the figure). The streamlines for the latter two cases begin at the stagnation line on the leading edge and travel down and around the cylindrical surface away from the stagnation line. The angle at which the flow travels down the leading edge before going around the side increases with the fin sweep angle since the bow shock acts like an oblique shock.

Within the interaction region, the streamlines turn upward to follow the shear layer that travels almost parallel to the surface of the test article geometry in the zoomed-in right image. Streamlines below the interaction turn up at an angle as the free-stream flow passes through the incident shock, and then also turn up after crossing the bow shock. This behavior of the streamlines is similar to the behavior for a comparable case in [8].

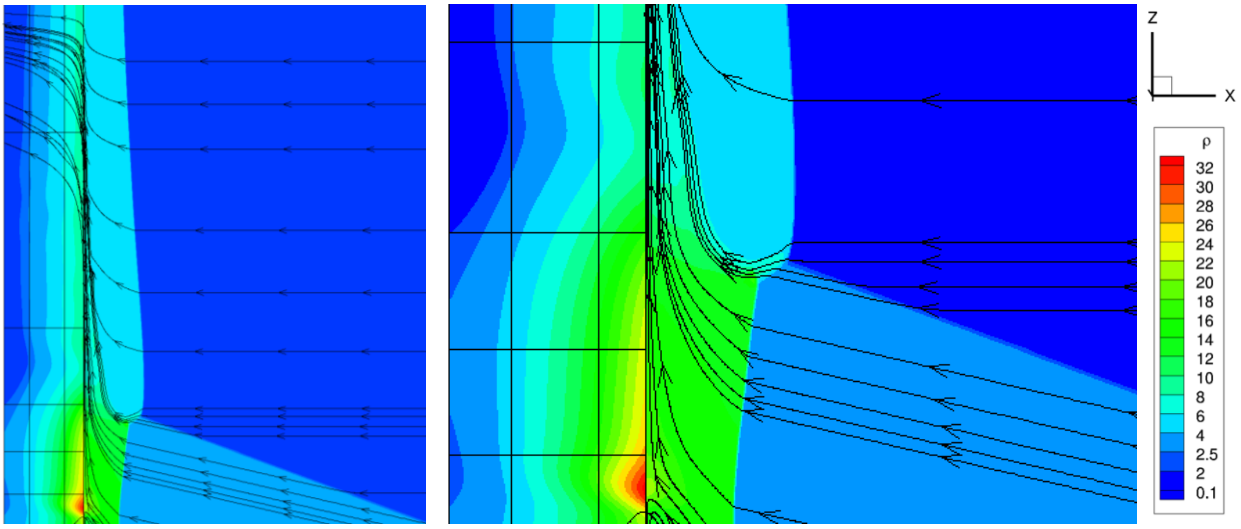

Figure 16. Density contour maps with streamlines along an leading edge for the 0.25 in-radius test article at a 0° AoA (from the LAURA simulation).

Similar comparisons of the streamlines in the interaction region for the -15° and -25° AoA cases were performed, but these images are not shown here. The density fluctuation in the flow for the Type IV interaction is represented by the streamlines in a vortical shape with the same direction of rotation as in [8], with flow moving up the leading edge near the surface and down farther out into the flow. This flow feature initially is close to the incident shock but moves higher relative to the leading edge as the simulation progresses before dissipating altogether, possibly due to the lower grid resolution above the incident shock. The streamlines for the Type III interaction show the rotating flow that causes the shear layer to detach from the surface of the test article, as in [8].

4. Conclusions

The Type IVa (0° AoA), direct Type IV (-15° AoA), and Type III (-25° AoA) shock-shock interactions were investigated using a test article geometry with a 0.25 in leading edge radius. Flow density gradients were modeled using a numerical schlieren technique to compare the results to experimental zoom schlieren data in [3]. The streamlines in the computationally modeled flow were also compared to the experimental oil flow images used to visualize the surface flow. The general heating behavior for these three interactions were assessed using LAURA, which neglects conduction through the geometry, and compared to IHEAT contour maps that represent mean heat transfer coefficients assuming 1D conduction.

Qualitatively, the heat transfer profiles from the LAURA output for each case are similar to the IHEAT contour maps of heat transfer coefficients. However, the peak region behavior for the Type III and Type IV interactions is less steady in the CFD simulations than in the phosphor thermography images. Based on the observations from this study, the Type IVa shock-shock interaction exhibits the smallest peak heating augmentation, at least in part due to the fact that the shear layer curls upward before attaching to the surface, rather than the full supersonic jet impinging directly on the surface of the test article. The Type IV interaction produces a narrow, steep heat transfer peak due to an impinging supersonic jet. The Type III interaction does not include a supersonic jet as in the other two cases, but instead yields a broader peak heat transfer region at the shear layer attachment point. The computational results indicate the peak vanishes and reappears during a time-accurate simulation, likely due to the shear layer detaching and reattaching to the surface of the test article.

The features exhibited in the simulated numerical schlieren videos (from the LAURA simulations) and the experimental zoom schlieren videos are mostly similar, except for the non-physical “wedge” in the flow parameters in the stagnation plane between the incident shock and a horizontal line (relative to the grid oriented at the test article angle of attack). This triangular region of different flow properties exists in the solutions for all three angles of attack, but only noticeably affects the flow to yield non-physical behavior in the Type IVa interaction. The curled-up shear layer and the narrow supersonic jet leaving the triple point are both visible in the numerical schlieren images for this case, once the interaction is fully set up in the simulation, but the numerical schlieren also indicates additional density gradients within the bow shock and a strange bow shock shape compared to the experimental zoom schlieren results. For the Type IV interaction, the shock train (shock triangles formed by reflected shocks within the supersonic jet) and the unsteady density gradient above the incident shock are distinguishable features in

the videos acquired with the computational and experimental schlieren techniques. The numerical schlieren videos show the changes in the position of the shear layer relative to the surface of the test article and the vortices moving down in the flow near the leading edge for the Type III interaction more clearly than the experimental zoom schlieren images. The general shape of the streamlines near the leading edge for the LAURA simulation with the test article at a 0° AoA is similar to streamlines on the oil flow test articles and in [8].

References

1 Andreadis, Dean. *Scramjet Engines Enabling the Seamless Integration of Air & Space Operations*. Pratt & Whitney, West Palm Beach, FL.

2 Edney, Barry. *Anomalous Heat Transfer and Pressure Distributions on Blunt Bodies at Hypersonic Speeds in the Presence of an Impinging Shock*. The Aeronautical Research Institute of Sweden, Stockholm, 1968.

3 Jones, Michelle L. and Berry, Scott A. Thermographic phosphor measurements of shock-shock interactions on a swept cylinder. (Daytona Beach, FL 2013), TFAWS.

4 Nowak, R., Holden, M., and Wieting, A. Shock/shock interference on a transpiration cooled hemispherical model. (Seattle, WA June 1990), AIAA 1990-1643.

5 Stewart, James R., Thareja, Rajiv R., Wieting, Allan R., and Morgan, Ken. Application of Finite Element and Remeshing Technique to Shock Interference on a Cylindrical Leading Edge. (Reno, Nevada 1988), AIAA 1988-0368.

6 Wieting, A. Shock interference heating in scramjet engines. (Orlando, FL October 1990), AIAA 1990-5238.

7 Vemaganti, G. and Wieting, A. Application of a Finite Element Algorithm for High Speed Viscous Flows Using Structured and Unstructured Meshes. (Seattle, WA June 1990), AIAA 1990-1648.

8 Wright, M. J., Nowak, R. J., Berry, S. A., Glass, C. E., and Candler, G. V. Numerical/Experimental Investigation of 3-D Swept Fin Shock Interactions. (Albuquerque, NM June 1998), AIAA 1998-2816.

9 Berry, Scott A. and Nowak, Robert J. Fin Leading-Edge Sweep Effect on Shock-Shock Interaction at Mach 6. *Journal of Spacecraft and Rockets*, 34, 4 (July-August 1997), 416-425.

10 Mazaheri, A., Gnoffo, P. A., Johnston, C. O., and Kleb, B. *LAURA Users Manual: 5.4-54166*. May 2011.

11 Jones, Michelle L. *Experimental Investigation of Shock-Shock Interactions over a 2-D Wedge at M = 6*. Virginia Polytechnic Instititute and State University, Hampton, VA, 2013.

12 Micol, J. R. Langley Aerothermodynamics Facilities Complex: Enhancements and Testing Capabilities. (Reno, NV Jan. 1998), AIAA 1998-0147.

13 Rhode, Matthew N. and DeLoach, Richard. Hypersonic Wind Tunnel Calibration Using the Modern Design of Experiments. (Tucson, AZ 2005), AIAA 2005-4274.

14 Merski, N. R. Reduction and Analysis of Phosphor Thermography Data with the IHEAT Software Package. (1997), AIAA 1998-0712.

15 Merski, N. R. Global Aeroheating Wind-Tunnel Measurements Using Improved Two-Color Phosphor Thermography Method. *Journal of Spacecraft and Rockets*, 36, 2 (March-April 1999), 160-170.

16 Devenport, William J. and Ford, Adam. *Compressible Aerodynamics Calculator*. Department of Aerospace and Ocean Engineering, Virginia Tech [online resource], Blacksburg, VA, [updated 2012, cited Mar 2013]. URL: http://www.dept.aoe.vt.edu/~devenpor/aoe3114/calc.html.

17 Fay, J. A. and Riddell, F. R. Theory of Stagnation Point Heat Transfer in Dissociated Air. *Journal of the Aeronautical Sciences*, 25, 2 (February 1958), 73-85, 121.

18 Hiers, Robert S. and Loubsky, William J. *Effects of Shock-Wave Impingement on the Heat Transfer on a Cylindrical Leading Edge*. NASA, Washington, D.C., 1967.